Research Article

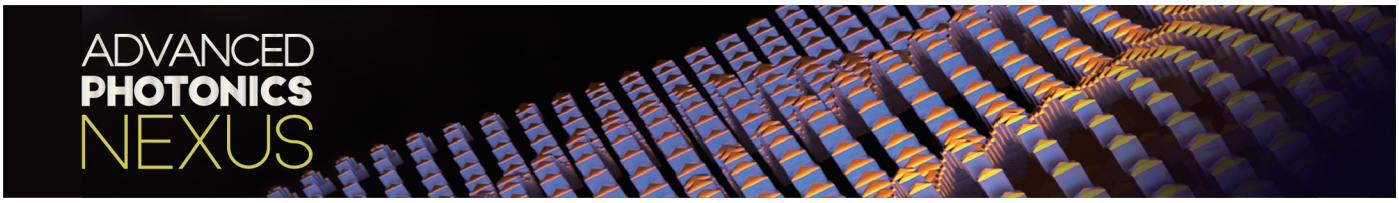

Ultrahigh rejection microring resonator assisted by an all-pass filter

Ming Chen,[a,†] Yifan Liu,[a,†] Kaixiang Cao,[a] Yuan Yu,[a,b,*] Fangzheng Zhang,[c] and Xinliang Zhang[a,b]

[a]Huazhong University of Science and Technology, Wuhan National Laboratory for Optoelectronics, and School of Optical and Electronic Information, Wuhan, China

[b]Optics Valley Laboratory, Wuhan, China

[c]Nanjing University of Aeronautics and Astronautics, National Key Laboratory of Microwave Photonics, Nanjing, China

Abstract. The microring resonator (MRR) plays an important role in signal processing because high-quality bandpass filtering can be obtained at its drop port. To promote the signal-to-noise ratio, a high rejection ratio is significantly demanded. However, it is still challenging to promote the rejection ratio of the MRR-based bandpass filter. To solve this problem, we propose to use an all-pass filter to enhance the rejection ratio of the MRR-based bandpass filter. Experimental results show that the improved rejection ratio is as high as 47.7 dB, which is improved by 23.6 dB compared with that of the MRR. Meanwhile, the bandwidth of the MRR-based bandpass filter is reduced from 2.61 to 1.14 GHz due to the constructive interference in the passband. In addition, the center frequency of this ultrahigh rejection MRR can be continuously tuned from 6.26 to 46.25 GHz. The quality factor (Q) of the MRR is improved from 7.4×10^4 to 1.7×10^5. During the adjustment, the rejection ratio of the bandpass filter exceeds 40 dB. The proposed approach can be used to achieve optical bandpass filters with high performance.

Keywords: microring resonator; all-pass filter; high rejection ratio.

Received Jun. 30, 2024; revised manuscript received Sep. 7, 2024; accepted for publication Oct. 14, 2024; published online Nov. 9, 2024.

[DOI: 10.1117/1.APN.3.6.066011]

1 Introduction

With the development of photonic integrated circuit technology, integrated optical filters have become a hot research topic.[1–7] Silicon-based microring resonators (MRRs) are ideal units for realizing large-scale integrated optical circuits due to their compact size, flexible function configuration, and excellent filtering performance.[8–11] In addition, both bandpass and bandstop filtering shapes can be obtained at the drop and through ports of the MRR, respectively. As is known, in an optical filter, a high rejection ratio is desired to significantly improve the signal-to-noise ratio and eliminate interferences completely. Therefore, much effort has been paid to improve the filter rejection.

As is known, optical interferometry has been previously used to enhance the rejection ratio of MRRs.[7,12] To improve the rejection ratio of the MRR at its through port, which is a bandstop filter, the approach of employing two cascaded tunable Mach–Zehnder interferometers (MZIs) is proposed.[13] By adjusting microheaters to equalize the amplitudes and obtain a precise π phase difference between the two sidebands in the two arms of the MZI, destructive interference is realized. Hence, the rejection ratio of the obtained MRR at its through port is increased to exceed 60 dB. To realize a high rejection ratio and reconfigurable optical bandstop filter, three-waveguide-coupled Sagnac loop reflectors are proposed.[14] The bus waveguides situated between the Sagnac loop reflectors introduce an additional feedback path for coherent optical interference. By adjusting the coherent mode interference within the device, the rejection ratio of the filter is significantly enhanced. However, the device complexity is significantly increased and cannot be fabricated in the foundry. However, compared with the MRR-based bandstop filter, it is more challenging to achieve a high rejection MRR at its drop port, which is a bandpass filter. This is because the interferences in a much larger spectral range must be eliminated. To enhance the rejection ratio of MRR at its through port, it was

*Address all correspondence to Yuan Yu, yuan_yu@hust.edu.cn

†These authors contributed equally to this work.

proposed to use a pair of cascaded MRRs combined with optical phase modulation. By employing amplitude cancellation in the stopband, the rejection ratio is increased.[15] However, the proposed approach is only applied to a microwave photonic filter and cannot increase the rejection of the MRR-based optical filter. In addition, the rejection ratio of this filter is only 20 dB. To realize a flat-top, high-rejection-ratio optical bandpass filter, an integrated photonic chip consisting of a 10th-order MRR and a photodetector (PD) is proposed.[16] By controlling the resonant wavelength of each MRR, the 10th-order MRR achieves a flat-top optical filter at its drop port, and the rejection ratio is higher than 30 dB. However, it is difficult to design and control the operation state of each MRR, and the complexity of the system is increased significantly. To improve the rejection ratio of MRR-based bandpass filters, high-order optical bandpass filters based on multi-MRRs have been proposed, such as using coupled resonator optical waveguides (CROWs)[17–19] or cascaded MRRs.[20] However, the rejection improvement is related to the number of employed MRRs. To achieve a high rejection ratio, multiple MRRs are used. Therefore, both the insertion loss and system complexity are significantly increased. How to improve the rejection ratio of the MRR-based bandpass filter is still a challenge.

In this paper, we propose to use an all-pass filter (APF) to enhance the rejection ratio of an MRR-based optical bandpass filter. With the assistance of APF, constructive interference occurs in the passband, and destructive interference occurs in the stopband of the optical bandpass filter simultaneously. Therefore, the rejection ratio of the optical bandpass filter can be significantly promoted. In the experiment, the rejection ratio of the MRR-based optical bandpass filter is increased from 24.1 to 47.7 dB compared with that of a single MRR. Meanwhile, due to the constructive interference in the center of the passband, the bandwidth of the bandpass filter is reduced from 2.62 to 1.14 GHz. The quality factor (Q) of the MRR is improved from 7.4×10^4 to 1.7×10^5. In addition, the center frequency of this bandpass filter can be continuously tuned from 6.26 to 46.25 GHz. Therefore, the proposed approach can effectively improve the performance of the MRR, thus enhancing the performance of optical systems.

2 Methods

2.1 Principle

Figure 1 shows the principle of the ultrahigh rejection MRR. Figure 1(a) illustrates the schematic structure of the MRR. The APF has a constant amplitude response and a phase change of 2π in a free spectral range (FSR),[21] as shown in Fig. 1(b). The amplitude and phase responses from the "input port" to the "drop port" of the MRR (MRR_{Drop}) are shown as the blue solid curve and the red dashed curve in Fig. 1(b), respectively.[22] We can see that the frequency response of MRR_{Drop} is a bandpass filter with a phase change of π in an FSR. Therefore, the frequency response of the cascaded APF and MRR_{Drop} is a bandpass filter ($APF \times MRR_{Drop}$) with a phase change of 3π in an FSR. Then, the frequency response of the cascaded APF and the MRR-based bandpass filter is superimposed with the frequency response of the MRR-based bandpass filter, as shown in Fig. 1(c). It should be noted that the two frequency responses have the same amplitude frequency response but different phase frequency responses. The phase difference between the two frequency responses is 0 at the center of the passband and tends to be π as the frequency deviates away from the passband center. Therefore, constructive interference occurs in the passband and destructive interference occurs in the stopband. As a result, the rejection ratio of the optical bandpass filter (MRR_{Final}) can be improved and the bandwidth is reduced, as shown in Fig. 1(c).

The schematic diagram of the proposed ultrahigh rejection bandpass filter assisted by APF is shown in Fig. 2. We can

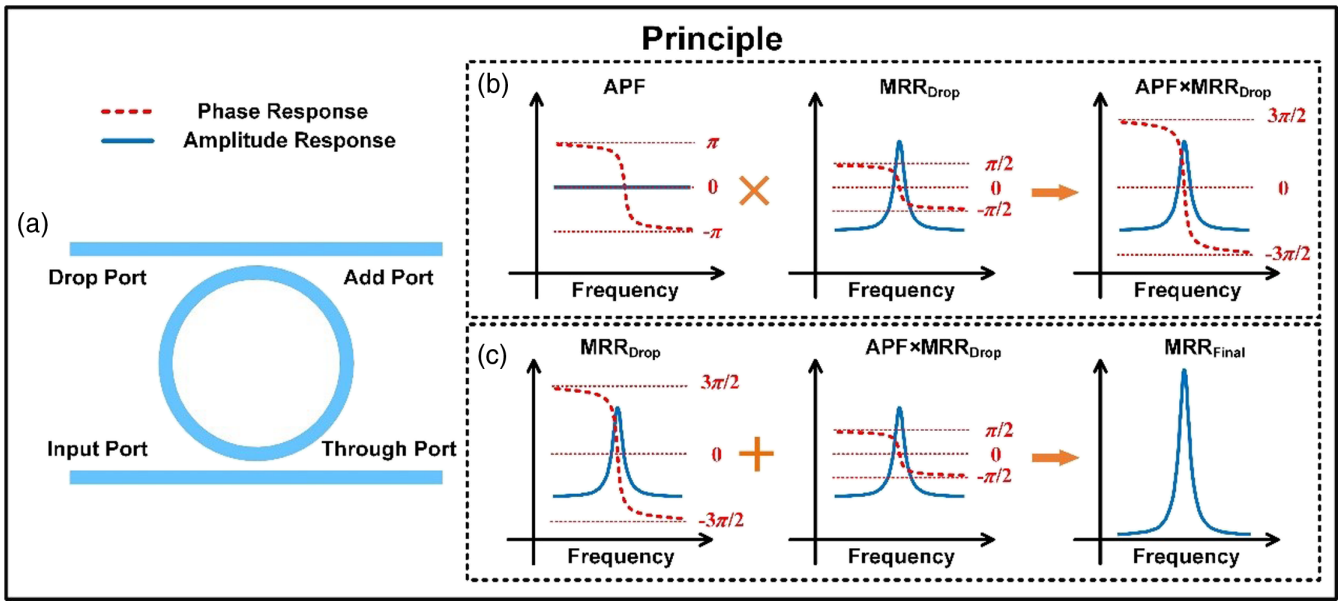

Fig. 1 Principle of the ultrahigh rejection MRR. (a) The schematic diagram of the MRR. (b) The frequency responses of the cascaded APF and MRR-based bandpass filter. (c) The principle of the ultrahigh rejection MRR. APF, all-pass filter (the blue solid curve shows the amplitude response and the red dashed curve shows the phase response).

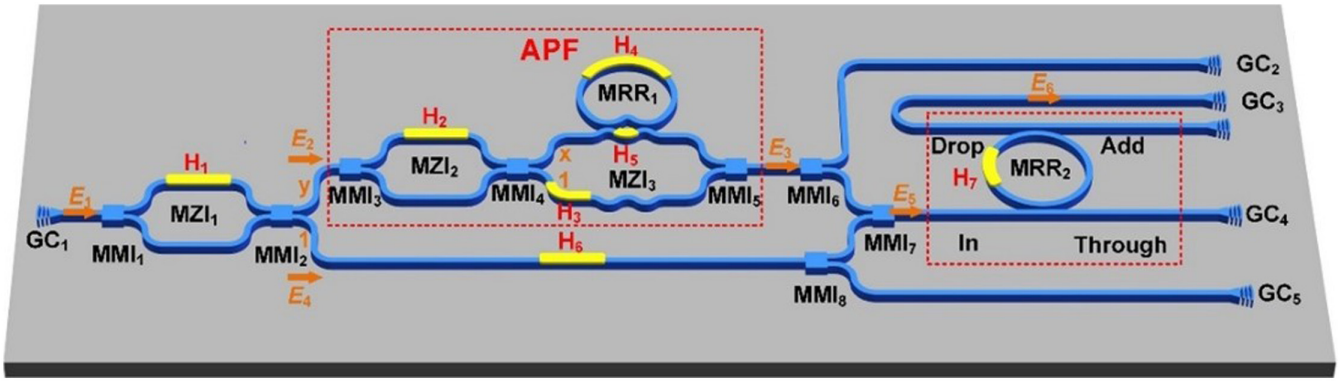

Fig. 2 Schematic diagram of the proposed ultrahigh rejection ratio MRR assisted by the APF. GC, grating coupler; MZI, Mach–Zehnder interferometer; MRR, microring resonator; MMI, multimode interferometer.

see that the proposed device mainly consists of an MZI, an APF, a parallel straight waveguide, and an MRR. The optical signal is coupled into the photonic chip through a grating coupler (GC_1), and the optical field is donated by E_1, as shown in Fig. 2. Then, the input optical field E_1 is divided into two parts by MZI_1, whose amplitude splitting ratio can be adjusted by controlling the electrical heating power applied to the microheater H_1. The optical field of the upper part is denoted by E_2. Then, the upper part passes through the APF, which consists of MZI_2, MZI_3, and MRR_1. The optical amplitude splitting ratio of MZI_2 can be adjusted by controlling the electrical heating power applied to the microheater H_2. In MZI_3, the optical field in the upper arm is coupled with MRR_1, and the microheaters H_4 and H_5 are used to adjust the resonant wavelength of MRR_1 and the coupling coefficient between MRR_1 and the upper arm of MZI_3, respectively. On the lower arm of MZI_3, the microheater H_3 is used to adjust the phase difference between the two arms of MZI_3. Notably, all the MZIs in the proposed device have a balanced structure. The optical field output from the APF is denoted by E_3. Meanwhile, the optical field at the lower output port of MZI_1 is denoted by E_4.

Based on the transmission matrix, the transfer function of the APF is given by

$$H_{\mathrm{APF}}=\frac{\sqrt{2}}{4}(1+je^{j\varphi_2})\frac{[(t_0+xe^{j\varphi_3})-\alpha(1+t_0xe^{j\varphi_3})e^{-\phi_1}]}{1-\alpha t_0e^{-\phi_1}}, \quad (1)$$

where φ_1, φ_2, and φ_3 are the phase differences between the upper and lower arms of MZI_1, MZI_2, and MZI_3, respectively. t_0 is the self-coupling coefficient between the upper arm of MZI_3 and MRR_1, α is the round-trip amplitude transmission of MRR_1, and ϕ_1 is the round-trip phase shift of the MRR_1. The optical amplitude splitting ratio x of the upper arm to the lower arm of MZI_3 is related to φ_2, where x satisfies $x=(j+e^{j\varphi_2})/(1+e^{j\varphi_2})$. According to the all-pass condition,[21] the transmission T of the APF can be expressed as

$$T=H_{\mathrm{APF}}\times H_{\mathrm{APF}}^{*}=\frac{(1+\cos\varphi_2)\alpha^2(1-t_0^2)^2}{2(1-\alpha^2t_0^2)^2}. \quad (2)$$

From Eq. (2), we can find that the amplitude frequency response is constant, and thus an APF is obtained. Meanwhile, the lower output of MZI_1 passes through a straight waveguide. The output signal of APF is divided into two parts by MMI_6. One part is output from the chip through GC_2 for facilitating the experiment, and the other part is combined with one part of the optical signal from the lower output arm of MZI_1 by MMI_7. The other part of the optical signal from the lower output arm of MZI_1, which is coupled out of the chip by GC_5, is also used to facilitate the experiment. The output optical field through MMI_7 is donated by E_5, and then coupled with MMR_2. The optical field at the "drop" port of MRR_2 is donated by E_6, which is coupled out of a chip by GC_3. Notably, the transmission and the phase shift from the "In" port to the "Drop" port of MRR_2 can be expressed as[20]

$$H_{\mathrm{Drop}}=\frac{-k_1k_2\alpha^{\frac{1}{2}}e^{-j\frac{\phi_2}{2}}}{1-\alpha t_1t_2e^{-j\phi_2}}, \quad (3)$$

where t_1 and t_2 are the self-coupling coefficients of the upper and lower coupling regions of MRR_2, respectively, and k_1 and k_2 are the cross-coupling coefficients of the upper and lower coupling regions of MRR_2, respectively. Neglecting the coupling loss, we can obtain $t_1^2+k_1^2=1$, $t_2^2+k_2^2=1$. α is the round-trip amplitude transmission of MRR_2 and ϕ_2 is the round-trip phase shift of the MRR_2. Neglecting the losses caused by MMI_5, MMI_6, MMI_7, and MMI_8, the transfer function of the proposed ultrahigh rejection bandpass filter can be expressed as

$$\begin{aligned}H_{\mathrm{BPF}}&=\frac{1}{\sqrt{2(1+y^2)}}(1+yH_{\mathrm{APF}})\,H_{\mathrm{Drop}}\\&=\frac{1}{\sqrt{2(1+y^2)}}(H_{\mathrm{drop}}+yH_{\mathrm{APF}}H_{\mathrm{drop}}).\end{aligned} \quad (4)$$

The optical amplitude splitting ratio of the upper arm to the lower arm of MZI_1 is assumed to be $y:1$, where y satisfies $y=(j+e^{j\varphi_1})/(1+e^{j\varphi_1})$. According to Eq. (4), we can see that the frequency response of the proposed structure can indeed be regarded as the superposition of the frequency response of the MRR_2-based bandpass filter (H_{Drop}), and the frequency response of cascading the APF with the MRR_2-based bandpass filter ($H_{\mathrm{Drop}}\times H_{\mathrm{APF}}$). As is known, the frequency response H_{Drop} exhibits a Lorentzian bandpass shape with a phase variation of π in an FSR. The frequency response $H_{\mathrm{Drop}}\times H_{\mathrm{APF}}$ has

the same shape as that of H_{Drop} but with a phase variation of 3π. We can align the resonant wavelengths of MRR_1 and MRR_2 by adjusting electrical powers applied to the microheater H_4 on MRR_1 and H_7 on MRR_2, respectively. Therefore, after superposition, the phase difference between the two frequency responses is 0 in the center of the passband and tends to be π as deviating from the center of the passband. When the deviation is FSR/2, the phase difference is π. Hence, constructive interference occurs in the passband and destructive interference occurs in the stopband of the bandpass filter. Consequently, a high rejection bandpass filter can be realized.

To validate our theory, we carry out simulations on the proposed device. In simulation, the three self-coupling coefficients of MRR_1 and MRR_2 are assumed to be $t_0 = 0.98$, $t_1 = 0.98$, and $t_2 = 0.98$, respectively. Both circumferences of the two MRRs are set as 251.2 μm. In addition, the silicon waveguide propagation loss is assumed to be 1.5 dB/cm. The simulated results are shown in Fig. 3. Figure 3(a) shows the simulated amplitude (black solid curve) and phase (yellow dashed curve) responses of the APF, which is indicated by the red dashed rectangle in Fig. 2. Notably, the APF can be realized at arbitrary self-coupling coefficient value of t_0 as long as the zero and pole satisfy Eq. (4).[23] It can be observed that the phase response of the APF has a phase variation of 2π in an FSR. The comparisons of the phase and amplitude responses of H_{Drop} (blue dashed curve) and $H_{\mathrm{Drop}} \times H_{\mathrm{APF}}$ (green solid curve) are shown in Figs. 3(b) and 3(c), respectively. It can be observed that the rejection ratio and the phase variation in an FSR of MRR_2-based bandpass filter are 33.8 dB and π, respectively. Notably, the amplitude responses of H_{Drop} and $H_{\mathrm{Drop}} \times H_{\mathrm{APF}}$ have exactly the same shape except for the insertion loss, which is caused by the insertion loss of the APF, as shown in Fig. 3(b). However, it is important to ensure that the insertion losses of the two bandpass filters are equal to each other, which can maximize the benefits of the optical interference. Therefore, to offset the insertion loss, we can adjust the power-splitting ratio of MZI_1 by changing the electrical power applied to H_1, as shown in Fig. 1. Meanwhile, the phase difference between H_{Drop} and $H_{\mathrm{Drop}} \times H_{\mathrm{APF}}$ is 0 at the passband center and tends to be π as the frequency deviates from the center of the passband. When the deviation from the passband center is FSR/2, the phase difference is π. As a result, after superimposing the frequency response of H_{Drop} and $H_{\mathrm{Drop}} \times H_{\mathrm{APF}}$, constructive interference occurs in the passband, and destructive interference occurs in the stopband simultaneously. Figure 3(d) shows the simulated results of our proposed ultrahigh rejection MRR. The simulated results show that the rejection ratio of MRR_2 is significantly improved with the assistance of the APF. When the wavelength deviates the resonance center of the MRR_2 by 0.5 nm, the rejection ratio can be improved from 28.9 to 64.0 dB. Meanwhile, thanks to

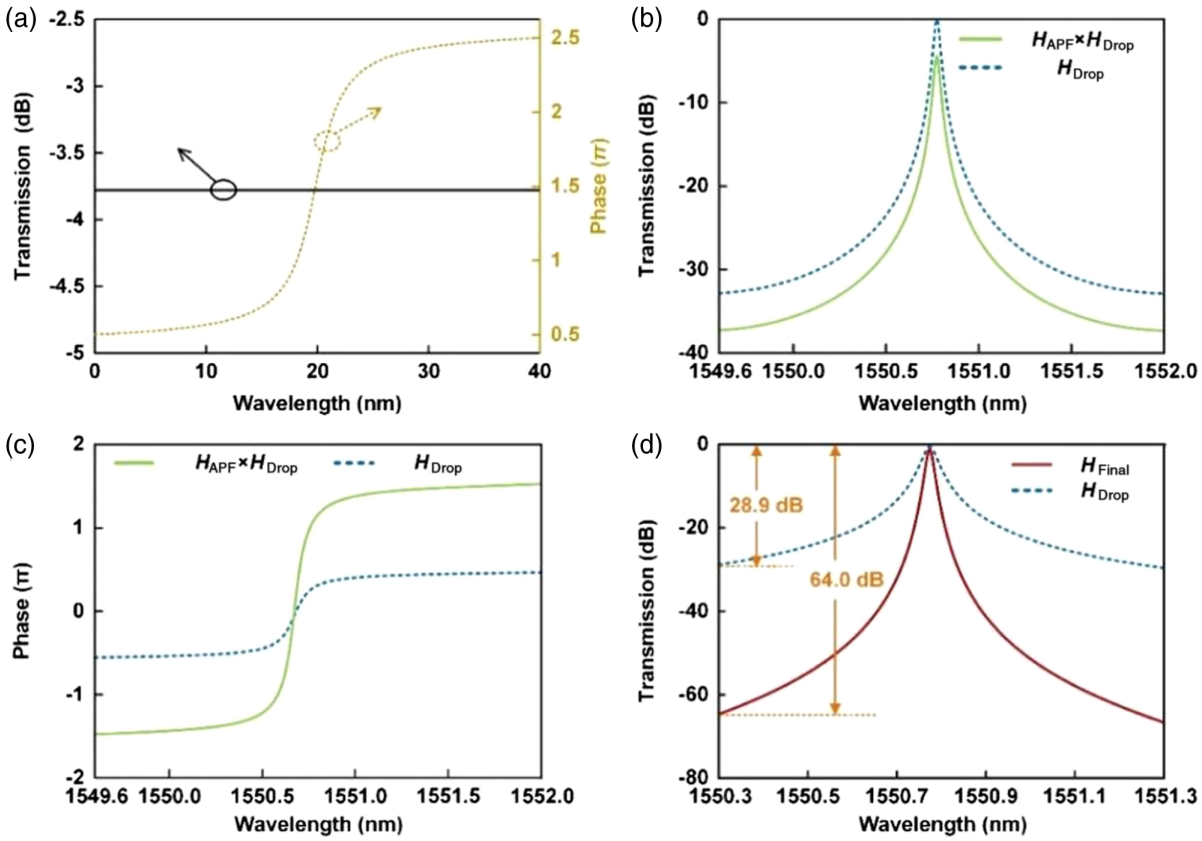

Fig. 3 Simulated results of the proposed device. (a) The amplitude (black solid curve) and the phase (yellow dashed curve) frequency responses of the APF. (b) The amplitude-frequency responses of H_{Drop} (blue dashed curve) and $H_{\mathrm{Drop}} \times H_{\mathrm{APF}}$ (green solid curve). (c) The phase frequency responses of H_{Drop} (blue dashed curve) and $H_{\mathrm{Drop}} \times H_{\mathrm{APF}}$ (green solid curve). (d) The amplitude frequency responses at the drop port of MRR_2 without (blue dashed curve) and with (red solid curve) APF.

constructive interference at the passband, the bandwidth is reduced from 2.36 to 1.11 GHz simultaneously.

2.2 Chip Fabrication

The chip is fabricated by Chongqing United Micro-Electronics Center (CUMEC), as shown in Fig. 2. According to Fig. 2, the proposed device is fabricated based on a silicon-on-insulator (SOI) wafer, which has a top layer thickness of 220 nm and a buried oxide (BOX) layer thickness of 2 μm. The waveguide width and etching depth are 500 and 150 nm, respectively. Figure 4 shows the micrograph of the fabricated device. The coupling gaps between the directional couplers in MZI_1, $MZ1_2$, and MZI_3 are all 200 nm. The titanium nitride (TiN) material deposited on the waveguide is used as the microheater. In addition, the microheaters deposited on the MZIs, optical straight waveguides, and MRRs are used to adjust the optical splitting ratio, the optical phase, and the resonant wavelengths of the MRRs, respectively. Both circumferences of the two MRRs are set as 251.2 μm. In addition, there are 16 pads fabricated on the chip for applying electrical power to the microheaters. The size of the whole device is 2.35 mm $\times$ 0.95 mm.

2.3 Experimental Setup

Due to the limited resolution of the optical spectrum analyzer, we perform the microwave photonic approach to measure the frequency responses of the proposed device precisely, as shown in Fig. 5. Another advantage of the microwave photonic measurement is that the phase response of the device can be obtained. As shown in Fig. 5, the continuous wave (CW) light at 1550 nm emitted from the tunable laser source (TLS, NKT Basik E15) is split into two parts by an optical coupler (OC_1). One part of the CW light is phase-modulated by the microwave signal emitted by a vector network analyzer (VNA, Anritsu MS4647B) via a phase modulator (PM, Covega Mach-40). Since the PM is polarization-dependent, a polarization controller (PC_1) is used to align the state of polarization (SOP) of the CW light with the polarization axis of the PM to ensure maximal modulation efficiency. Then the +1st-order

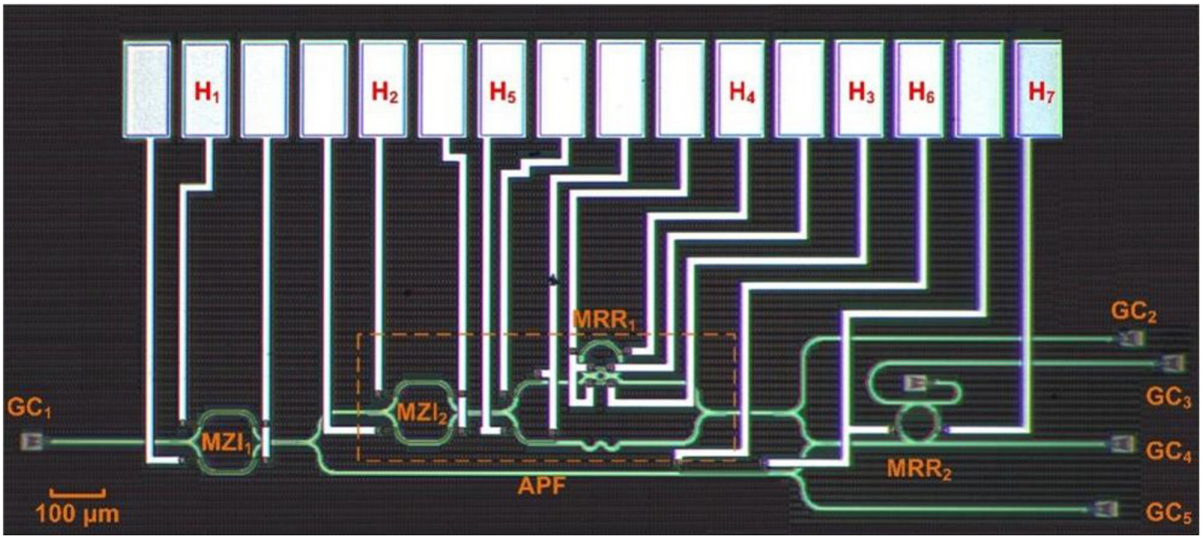

Fig. 4 Micrograph of the fabricated device. GC, grating coupler; MZI, Mach–Zehnder interferometer; MRR, microring resonator; MMI, multimode interferometer; APF, all-pass filter.

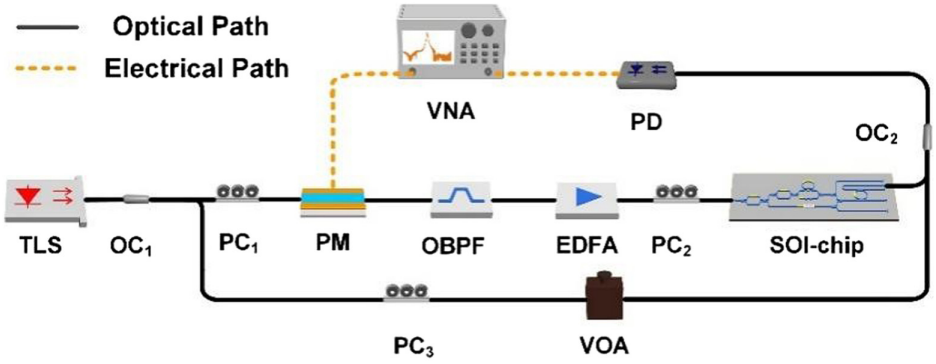

Fig. 5 The experimental setup for precisely measuring the amplitude and phase responses of the fabricated device. TLS, tunable laser source; OC, optical coupler; PC, polarization controller; PM, phase modulator; OBPF, optical bandpass filter; EDFA, erbium-doped fiber amplifier; VOA, variable optical attenuator; PD, photodetector; VNA, vector network analyzer.

sideband of the phase-modulated signal is suppressed by an optical bandpass filter (OBPF) to obtain a single sideband (SSB) signal. An erbium-doped fiber amplifier (EDFA) is used to boost the optical power. Notably, the fabricated device is polarization-dependent because of the difference in vertical and horizontal dimensions. Therefore, to maximize the coupling efficiency, PC_2 is used to adjust the SSB signal to TE mode. After adjusting the SOP by PC_2, the SSB signal is coupled into the chip for sweeping the device under test (DUT). After processing, the optical signal is output out of the chip and combined with the optical carrier via OC_2. To achieve a polarization-independent chip, the thick silicon wafer can be used.[24,25] PC_3 is used to adjust the SOP of the optical carrier to be aligned with the SOP of the optical signal after DUT. A variable optical attenuator (VOA) regulates the optical power injected into a PD by adjusting the power of the optical carrier. Finally, the PD converts the optical signal back to the electrical signal and returns it to the VNA for measurement.

3 Results and Discussion

To measure the frequency response of the APF, we attenuate the optical carrier injected into OC_2 in Fig. 5 completely. Then, the splitting ratio of MZI_1 is adjusted by changing the electrical power applied to the microheater H_1 so that all the input CW light passes through the upper output of MZI_1, as shown in Fig. 1. Then, the amplitude and the phase differences between the upper and lower outputs of MZI_2 are adjusted by changing the electrical power applied to H_2 and H_3. The electrical powers applied to H_1, H_2, and H_3 are 38.0, 44.0, and 9.0 mW, respectively; the measured amplitude and phase responses of APF via GC_2 are shown as the black solid curve and the red dashed curve in Fig. 6(a), respectively. It can be observed that the amplitude variation of the optical APF is within 1.5 dB, and the phase variation from 5 to 40 GHz is 1.95π, respectively. Notably, the amplitude variation of the APF is mainly caused by the FP effect, which originates from the backreflection of GC_1 and GC_3.

To measure the amplitude response of MRR_2 from GC_3 without APF assistance, we adjusted the splitting ratio of MZI_1 to make all the optical signal transmitted along the lower output waveguide of MZI_1. When the electrical power applied to H_1 is 10.7 mW, the measured amplitude response of MRR_2-based bandpass filter via GC_3 is shown as the black curve in Fig. 6(b). It can be observed that the measured rejection ratio of the bandpass filter is only 24.1 dB, and the bandwidth of the bandpass filter is 2.61 GHz. To obtain a bandpass filter with an ultrahigh rejection ratio, the electrical power applied to the microheaters of the APF remains unchanged. Then, the electrical powers of the microheaters H_4 and H_7 applied to MRR_1 and MRR_2 are adjusted to align the resonant wavelengths of MRR_1 and MRR_2. Finally, the electrical powers of the microheaters H_1 and H_6 are adjusted to change the splitting ratio and the phase difference between the APF and the lower output straight waveguide of MZI_1. The powers applied to microheaters H_1, H_2, H_3, H_4, H_6, and H_7 are 38.0, 44.0, 6.0, 21.6, 59.3, and 15.2 mW, respectively; the measured amplitude-frequency response of the ultrahigh rejection optical bandpass filter via GC_3 is shown as

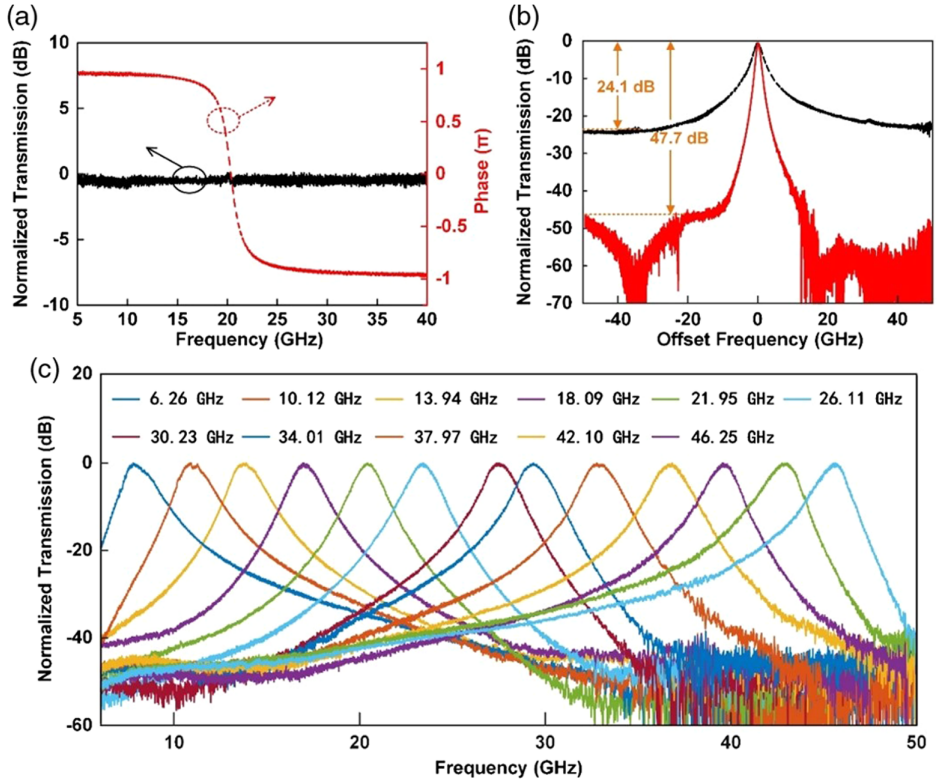

Fig. 6 Experimental results. (a) The amplitude (black solid curve) and phase (red dashed curve) frequency responses of the APF. (b) The amplitude-frequency response of MRR_2 without (black dashed curve) and with (red solid curve) the assistance of APF. (c) Tuning the center frequency of the MRR_2 with the assistance of APF.

the red solid curve in Fig. 6(b). We can observe that the measured rejection ratio of the bandpass filter is increased to as high as 47.7 dB with the assistance of the APF. Hence, the rejection ratio is improved by 23.6 dB compared with that of MRR_2. The insertion loss of the fabricated device is ~10 dB. It is mainly caused by the insertion loss introduced by the MMIs designed to assist the experiment and the insertion loss of the APF. In addition, we can see a notch around 35 GHz. This is because the upper arm and lower arm optical field propagation paths of MZI_1 are not precisely equal to each other. In addition, the measured bandwidth of the proposed structure is simultaneously reduced from 2.61 to 1.14 GHz with the assistance of the APF. The Q of the MRR is improved from 7.4×10^4 to 1.7×10^5. Because the phase difference between H_{Drop} and $H_{\mathrm{Drop}} \times \mathrm{H}_{\mathrm{APF}}$ is 0 in the passband center, constructive interference occurs at the center of the passband. When the phase difference in the passband between H_{Drop} and $H_{\mathrm{Drop}} \times H_{\mathrm{APF}}$ is not 0 because of frequency deviation, the amplitude enhancement due to optical interference is not so high. Therefore, the bandwidth of the optical bandpass filter is reduced. Furthermore, the bandpass filter with the ultrahigh rejection ratio can also be tuned by adjusting the resonant wavelengths of MRR_1 and MRR_2 simultaneously. This can be achieved by adjusting the electrical powers applied to H_4 and H_7, as shown in Fig. 6(c). Notably, the rejection ratio of the proposed device exceeds 40 dB during the tuning process. In our design, we sacrifice insertion loss and chip size to obtain a higher rejection ratio bandpass filter. Besides, a larger self-coupling coefficient of MRR_1 allows for a smaller bandwidth of the device. However, the insertion loss of the APF will be increased, and thus the insertion loss of the device will be increased. Therefore, trade-off considerations should be made among rejection ratio, bandwidth, integration, and insertion loss.

A comparison between previously reported integrated optical bandpass filters and this work is shown in Table 1. Our proposed ultrahigh rejection MRR assisted by APF exhibits a high rejection ratio. With the assistance of an APF, the rejection ratio is increased from 24.1 to 47.7 dB compared with that of a single MRR. In addition, the bandwidth of our proposed device is reduced by more than one-half of the bandwidth of the single MRR. Simultaneously, a large frequency tuning range is obtained while maintaining a narrow full width at half-maximum (FWHM) bandwidth. Further, the coupling region of MRR_2 can be designed with an adjustable coupling coefficient to reconfigure the bandwidth of the filter.

Table 1 Performance comparison of integrated optical bandpass filters.

Technology	Rejection ratio (dB)	Tuning range (GHz)	FWHW bandwidth (GHz)
SOI ring[16]	>30	5.3 to 19.5	NA
SOI CROWs[17]	>28.41	4 to 36	0.63 to 2.88
SOI disk[26]	15	3 to 10	1.93
SOI ring[27]	>10	3 to 21	0.36 to 0.47
SOI ring[28]	19.5	7.89 to 36.13	0.84
This work	47.7	6.26 to 46.25	1.14

NA, not available.

4 Conclusion

We have proposed and demonstrated an ultrahigh rejection MRR with the assistance of an APF. Due to the APF, we can obtain constructive interference in the passband and destructive interference in the stopband simultaneously. Therefore, the rejection ratio of the MRR is significantly increased. In the experiment, the rejection ratio of the optical bandpass filter is increased to as high as 47.7 dB, which is improved by 23.6 dB compared with that of the single MRR. In addition, the bandwidth of the MRR is also reduced from 2.61 to 1.14 GHz. With the assistance of the APF, the Q of the MRR is improved from 7.4×10^4 to 1.7×10^5. Meanwhile, the center frequency of ultrahigh rejection MRR can be continuously tuned from 6.26 to 46.25 GHz. The ultrahigh rejection ratio MRR proposed in this paper is implemented based on SOI. It is compatible with large-scale integrated photonic circuits. The proposed approach can potentially be applied to an important part of signal processing in large-scale integrated photonic circuits and provide different filtering functions to meet different requirements.

5 Appendix: Measuring the Frequency Response of MRR

We perform a microwave photonic link, as shown in Fig. 5, to measure the frequency response of MRR_2 by VNA. As both the bandwidths of PD and PM are 40 GHz, the measuring range of the VNA is also limited to 40 GHz, which corresponds to a wavelength range of 0.32 at 1550 nm. Hence, the measuring range of the microwave photonic approach is much less than the FSR of MRR_2, which is as large as approximately 300.0 GHz. To demonstrate the rejection ratio enhancement of MRR_2 with the assistance of APF, the measured frequency response of the MRR_2 by VNA must be spliced.[29] At first, the wavelength of the TLS is adjusted to 1549.66 nm, and the OBPF is adjusted to eliminate the +1st-order sideband of the phase-modulated light. Then, the transmission of MRR2 from 1549.50 to 1549.82 nm can be measured by the VNA, which corresponds to the frequency response from −50 to −10 GHz in Fig. 6(b). The next step is to adjust the wavelength of the TLS to 1549.98 nm; the OBPF is also adjusted correspondingly to eliminate the +1st-order sideband of the phase-modulated light. Then, the transmission of MRR_2 from 1549.82 to 1550.14 nm can be measured by the VNA, which corresponds to the frequency response from −10 to 30 GHz in Fig. 6(b). In a similar way, the frequency response of MRR_2 from 30 to 50 GHz in Fig. 6(b) can be measured by the VNA. Finally, the frequency response from −50 to 50 GHz of the MRR_2 as shown in Fig. 6(b) can be obtained by splicing the three measured transmission spectra by VNA.

Disclosures

The authors declare that there are no financial interests, commercial affiliations, or other potential conflicts of interest that could have influenced the objectivity of this research or the writing of this paper.

Code and Data Availability

The datasets used and/or analyzed in the current study are available from the corresponding author upon reasonable request.

Authors' Contributions

Y.F.L. and Y.Y. conceived the idea. M.C. and Y.F.L. designed and fabricated the chip. M.C., K.X.C., and Y.Y. designed and performed the experiment. Y.Y., M.C., K.X.C., and Y.F.L. discussed and analyzed the data. M.C. prepared the manuscript. Y.Y. and M.C. revised the paper. Y.Y., F.Z.Z., and X.L.Z. supervised the project. All authors read and approved the final manuscript.

Acknowledgments

This work was supported by the National Key Research and Development Program of China (Grant No. 2018YFA0704403), the National Natural Science Foundation of China (Grant No. 61975249), the Program for HUST Academic Frontier Youth Team (Grant No. 2018QYTD08), the Project of Key Laboratory of Radar Imaging and Microwave Photonics (Nanjing University of Aeronautics and Astronautics), Ministry of Education (Grant No. NJ20230001), and the Independent Innovation Foundation of HUST (Grant No. 5003187117).

References

1. J. Capmany et al., "A tutorial on microwave photonic filters," *J. Lightwave Technol.* **24**, 201–229 (2006).
2. Y. Dong et al., "Hybrid DFT-spread OFDM-digital filter multiple access PONs for converged 5G networks," *J. Opt. Commun. Networking.* **11**, 347–353 (2019).
3. C. K. Madsen, "Optical all-pass filters for polarization mode dispersion compensation," *Opt. Lett.* **25**, 878–880 (2000).
4. M. Jablonski et al., "The realization of all-pass filters for third-order dispersion compensation in ultrafast optical fiber transmission systems," *J. Lightwave Technol.* **19**, 1194–1205 (2002).
5. H. Folkert et al., "Cascaded Mach-Zehnder wavelength filters in silicon photonics for low loss and flat pass-band WDM (de-) multiplexing," *Opt. Express.* **21**, 11652–11658 (2013).
6. Y. Tao et al., "Hybrid-integrated high-performance microwave photonic filter with switchable response," *Photon. Res.* **9**, 1569–1580 (2021).
7. J. Xu et al., "Ultra-narrow passband-tunable filter based on a high-Q silicon racetrack resonator," *Opt. Lett.* **46**, 5575–5578 (2021).
8. H. Tang et al., "Wideband tunable optoelectronic oscillator based on a microwave photonic filter with an ultra-narrow passband," *Opt. Lett.* **43**, 2328–2331 (2018).
9. X. Kong et al., "Microwave photonic image-reject mixer based on a tunable microwave photonic filter with high rejection," *IEEE Photon J.* **10**, 1–11 (2018).
10. A. Velamuri et al., "Programmable silicon photonic RF filters with symmetric out-of-band rejection," *J. Lightwave Technol.* **42**, 1–12 (2024).
11. Z. Zhou et al., "Photonics in a time of rapid growth: silicon-based optoelectronics in China," *IEEE Photon J.* **16**, 1–9 (2024).
12. D. Marpaung et al., "Si_3N_4 ring resonator-based microwave photonic notch filter with an ultrahigh peak rejection," *Opt. Express* **21**, 23286–23294 (2013).
13. X. Liu et al., "Silicon-on-insulator-based microwave photonic filter with narrowband and ultrahigh peak rejection," *Opt. Lett.* **43**, 1359–1362 (2018).
14. H. Arianfard et al., "Three waveguide coupled Sagnac loop reflectors for advanced spectral engineering," *J. Lightwave Technol.* **39**, 3478–3487 (2021).
15. S. Song et al., "Tunable single-passband microwave photonic filter based on integrated optical double notch filter," *J. Lightwave Technol.* **36**, 4557–4564 (2018).
16. L. Xu et al., "Silicon-on-insulator-based microwave photonic filter with widely adjustable bandwidth," *Photon. Res.* **7**, 110–115 (2019).
17. Y. Liu et al., "Reconfigurable microwave photonic bandpass filter based on CROW," *J Lightwave Technol.* **42**, 1597–1604 (2024).
18. R. R. Kumar et al., "Compact high-extinction unable CROW filters for integrated quantum photonic circuits," *Opt. Lett.* **45**, 1289–1292 (2020).
19. R. R Kumar et al., "High-extinction CROW filters or scalable quantum photonics," *Opt. Lett.* **46**, 134–137 (2021).
20. Y. Liu et al., "Tunable and reconfigurable microwave photonic bandpass filter based on cascaded silicon microring resonators," *J. Lightwave Technol.* **40**, 4655–4662 (2022).
21. W. Jiang et al., "Optical all-pass filter in silicon-on-insulator," *ACS Photonics* **7**, 2539–2546 (2020).
22. X. Lu et al., "Silicon-on-insulator-based microwave photonic filter with widely adjustable bandwidth," *Photonics Res.* **7**, 110–115 (2019).
23. Y. Chen et al., "Reconfigurable second-order optical all-pass filter," *Nanophotonics* **11**, 3115–3125 (2022).
24. T. Aalto et al., "Open-access 3-μm SOI waveguide platform for dense photonic integrated circuits," *IEEE J. Sel. Top. Quantum Electron.* **25**, 1 (2019).
25. Y. Wang et al., "S- and C-band nanosecond 1×2 plasma dispersion 3-μm silicon MZI switch with low polarization sensitivity," in *OECC*, pp. 1–4 (2023).
26. W. Zhang et al., "On-chip silicon photonic integrated frequency-tunable bandpass microwave photonic filter," *Opt. Lett.* **43**, 3622–3625 (2018).
27. Y. Tao et al., "Hybrid integrated high-performance microwave photonic filter with switchable response," *Photonics Res.* **9**, 1569–1580 (2021).
28. W. Jiang et al., "Optical filter switchable between bandstop and bandpass responses in SOI wafer," *IEEE Photon. Technol. Lett.* **32**, 1105–1108 (2020).
29. S. Cui et al., "Compact microring resonator based on ultralow-loss multimode silicon nitride waveguide," *Adv. Photon. Nexus* **2**, 046007 (2023).

Ming Chen received his master's degree from the Wuhan National Laboratory for Optoelectronics, Huazhong University of Science and Technology (HUST), Wuhan, China, in 2024. His research interest is microwave signal processing.

Yifan Liu received his PhD from the Wuhan National Laboratory for Optoelectronics, HUST, Wuhan, China, in 2023. His research interest is microwave signal processing.

Kaixiang Cao received his master's degree from the Wuhan National Laboratory for Optoelectronics, HUST, Wuhan, China, in 2024. His research interest is microwave signal processing.

Yuan Yu (Member, IEEE) received his PhD in optoelectronic information engineering from the School of Optical and Electronic Information, HUST, Wuhan, China, in 2013. He is currently an associate professor at the Wuhan National Laboratory for Optoelectronics and the Institute of Optoelectronics Science and Engineering, HUST. His research interests include microwave photonics and silicon-based integrated devices.

Fangzheng Zhang (Senior Member, IEEE) received his BS degree from the HUST, Wuhan, China, in 2008, and his PhD from the Beijing University of Posts and Telecommunications, Beijing, China, in 2013. He is currently a professor at the College of Electronic and Information Engineering, Nanjing University of Aeronautics and Astronautics, Nanjing, China. His main research interests include microwave photonics, radar imaging, and machine learning.

Xinliang Zhang (Senior Member, IEEE) received his PhD in physical electronics from the HUST, Wuhan, China, in 2001. He is currently a professor at the Wuhan National Laboratory for Optoelectronics and the Institute of Optoelectronics Science and Engineering, HUST. His main research interests include information optoelectronic devices and integration.